ACS Catalysis

pubs.acs.org/acscatalysis Research Article

Earth-Abundant-Based Photocatalysts for Efficient and Selective H_2 Production through Reforming of Formic Acid under Visible Light

Houeida Issa Hamoud, Lukasz Wolski, Hanen Abdelli, Radhouane Chtourou, Oleg Lebedev, Christine Martin, Dong Fan, Guillaume Maurin, Antoine Maignan,* and Mohamad El-Roz*

Cite This: *ACS Catal.* 2023, 13, 16266−16278 Read Online

ACCESS | Metrics & More | Article Recommendations | Supporting Information

ABSTRACT: Hydrogen is considered one of the most promising future solar fuels. Nowadays, particular attention is directed to H_2 production through the photoreforming of formic acid (FAc). However, acceptable conversion of FAc into H_2 is usually observed only at relatively high temperatures or in the presence of expensive noble metal catalysts. In this study, Cu_2O was combined with selected semiconducting metal oxide, namely, CuO, CeO_2, Fe_2O_3, Cu−Fe−O spinel, Nb_2O_5, TiO_2, and Fe_3O_4, and applied for FAc dehydrogenation at room temperature under visible irradiation. It was found that the type of semiconductor has a significant impact both on the activity and reaction selectivity of the Cu_2O-based catalysts. A synergetic activity with the highest FAc conversion (9.89 $mmol \cdot g^{-1} \cdot h^{-1}$) and selectivity to H_2 (>99%) was observed for the Earth-abundant Cu_2O/Fe_3O_4 composite. This synergetic enhancement, with respect to monocomponent ones, originates from an efficient separation of the photogenerated charge carrier according to Z-scheme mechanism accompanied by an *in situ* restructuring of Cu_2O into Cu^0/Cu_2O. In addition, as-formed Cu^0 particles, resulting from the restructuring, are found to be an active component responsible for highly efficient H_2 production over Cu_2O/Fe_3O_4. The density functional theory calculations confirm this hypothesis and highlight the role of Cu^0 in the reaction mechanism.

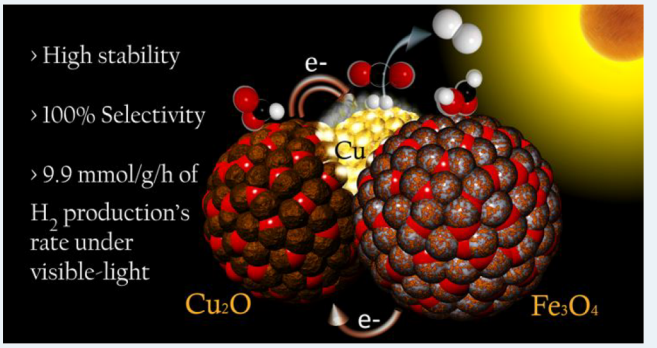

KEYWORDS: *formic acid, dehydrogenation, hydrogen, photocatalysis, copper, liquid organic hydrogen carrier (LOHC)*

1. INTRODUCTION

The fast depletion of fossil fuels and increasing pollution of the environment caused by their combustion have initiated intensive studies that search for new and more environmentally benign sources of energy. Nowadays, particular attention is directed to hydrogen, which is considered as one of the most promising future solar fuels because of its high energy density (~120 MJ/kg) and wide availability on Earth in the form of water, organic matter, and hydrocarbons.[1] To date, much effort has been undertaken to produce hydrogen via thermally driven processes in which decomposition of a given hydrogen source, such as liquid organic hydrogen carrier (LOHC), is catalyzed by supported metal species.[2] From among various LOHC, particular attention has been paid to the production of hydrogen from formic acid (FAc) because of its low toxicity, nonflammability, availability, high stability, and high H_2 volumetric capacity (53 $kg \cdot m^{-3}$).[3−5] Typically, catalytic decomposition of FAc proceeds via two ways: (1) dehydrogenation ($HCOOH \rightarrow H_2 + CO_2$) and (2) dehydration ($HCOOH \rightarrow CO + H_2O$).[6] So far, it has been documented that the former reaction can be conducted efficiently with high selectivity over various supported noble metals.[7−9] However, acceptable conversion of FAc into H_2 was usually observed mainly at relatively high temperatures.[7] In view of this drawback, as well as the high price and limited availability of noble metals, further studies in this field have been focusing on searching for an alternative and less expensive method for hydrogen production in which hydrogen is generated from a given source at low temperature with the use of catalysts based on Earth-abundant elements.[10] Particular attention is now directed to the development of photocatalytically driven processes in which iron- or copper-based nanomaterials are used as the active components. For instance, very recent studies indicate that Fe−Cu antenna reactor (AR) complexes may successfully catalyze a photoassisted dehydrogenation of NH_3 at 352 °C upon its exposure to visible light, reaching similar activity in H_2 production as that observed for ruthenium-based systems (Ru−Cu-AR complexes).[11] Thus, these results clearly show that iron, known for its low activity in a thermally driven NH_3 decomposition, is a promising abundant

Received: October 3, 2023
Revised: November 16, 2023
Accepted: November 16, 2023
Published: December 6, 2023

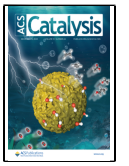

https://doi.org/10.1021/acscatal.3c04690
ACS Catal. 2023, 13, 16266−16278

element that can efficiently catalyze hydrogen production via a photocatalytic mechanism. Very recently, we investigated a copper iron spinel ($CuFe_2O_4$)-based catalyst for formic acid dehydrogenation under visible light. Despite the high activity of the materials assigned to a synergetic effect between the residue of tetrahedrally coordinated Cu species and the spinel support, the selectivity of the reaction was relatively low (around 70%).[12] On the other hand, it was documented that Cu_2O can catalyze selective transformation of FAc to H_2 and CO_2 without formation of CO as undesirable side product.[13] However, its efficiency in hydrogen production was found to be strongly limited because of a relatively fast recombination of photoexcited charge carriers (e^- and h^+). According to previous studies, this drawback of Cu_2O-based catalysts can be overcome by the formation of a heterojunction with other semiconductors characterized by appropriate valence and conduction band edges alignment.[13,14] To date, such an approach allowed for significant enhancement of Cu_2O activity in various photocatalytic processes by combination of copper oxide with selected wide band gap metal oxides (e.g., TiO_2,[15] CeO_2,[16] Nb_2O_5,[17] etc.) as well as other materials that can be activated under visible light (e.g., CuO,[18] Fe_2O_3,[19] Cu−Fe−O spinel[12] and Fe_3O_4,[20] etc.). The majority of studies involving copper-containing composites for hydrogen production via formic acid dehydrogenation are focused on liquid-phase dehydrogenation. However, in this scenario, the potential application of copper-based catalytic systems is severely limited due to the leaching of the active component under aqueous acidic conditions.[21] To address this limitation, the primary objective of our study is to explore various Cu_2O-semiconductor heterojunctions for the photocatalytic reforming of formic acid in the gas phase under visible light. This approach aims to overcome the challenges associated with aqueous acidic conditions and pave the way for efficient and selective hydrogen production using copper-based catalysts. The base hypothesis is that the selection of appropriate semiconductors, characterized by suitable valence and conduction band edges alignment, will improve the efficiency of charge carrier separation, resulting in fast restructuring of Cu_2O, enhancement of the activity, dehydrogenation-selectivity, and stability of Cu_2O-based nanocomposites under working conditions. The studies include the usage of well-known semiconducting metal oxides of different surface and optical properties, namely, CuO, CeO_2, Fe_2O_3, Cu−Fe−O spinel, Nb_2O_5, TiO_2, and Fe_3O_4, as a support/cocatalyst for Cu_2O. Deep insights into the possible reaction mechanisms over the various heterostructure catalysts, as well as the role of a given support/cocatalyst in controlling the photocatalytic activity of Cu_2O, are provided by monitoring the evolution of surface and gas-phase products formed during FAc decomposition by means of *operando* Fourier transform infrared (FTIR) spectroscopy coupled with mass spectrometry (MS).

2. EXPERIMENTAL SECTION

2.1. Materials. Copper(II) nitrate ($Cu(NO_3)_2{\cdot}3H_2O$; ≥99.99%), sodium hydroxide pellets (≥99.9%), and acetic acid (≥99.8%) were all purchased from Sigma-Aldrich. Two commercial iron oxides, Fe_3O_4 (99.99%) and Fe_2O_3 (99.5%), were used as received from Sigma-Aldrich and Alfa Aesar, respectively. Titanium dioxide (TiO_2 P25) was purchased from Degussa, and cerium dioxide (CeO_2) was supplied by GTRSA. Deionized water and absolute ethanol were used as solvents.

2.2. Catalyst Synthesis. The Cu_2O/semiconductor composites have been prepared by wet impregnation of the pure catalysts with a 1 to 1 weight ratio, followed by rigorous mechanical mixing and drying at 50 °C. All preparation and experiments are repeated, at least three times, in order to avoid any problem related to the heterogeneity of the catalysts. Below we report the synthesis procedures of the noncommercial metal oxides prepared in this study.

Synthesis of cuprospinel (Cu−Fe−O spinel): This sample, labeled Cu/Fe (1:3) in our previous work,[12] was synthesized by the starch-assisted sol−gel autocombustion method. The desired amounts of iron(III) nitrate and copper(II) nitrate were dissolved in deionized water to obtain a homogeneous solution. Then, an aqueous solution of starch $(C_6H_{10}O_5)_n$ was mixed with the metal-nitrate solution. The obtained mixture was heated at 100 °C under continuous stirring until the formation of a viscous brown gel. Then, the gel was heated at 180 °C for 4 h to initiate a self-sustaining combustion reaction and produce the precursor. The precursors were further ground to a powder and finally heated in air at 800 °C.

Synthesis of CuO: CuO was synthesized using a chemical precipitation method described elsewhere.[22] $Cu(NO_3)_2$ solution (300 mL, 0.02 M) was prepared and heated at 100 °C under vigorous stirring. Then, 0.5 g of solid NaOH was rapidly added resulting in the production of a considerable amount of black precipitate. Next, the precipitate was heated at 100 °C for 20 min under an ambient atmosphere. The resulting product was then centrifuged, washed with water and ethanol several times, and then dried in air at room temperature.

Synthesis of Cu_2O: The Cu_2O was synthesized using the hydrothermal method.[23] In a typical procedure, $Cu(NO_3)_2{\cdot}3H_2O$ (0.025 M) was dissolved in 30 mL of anhydrous absolute ethanol in a Teflon flask under vigorous stirring. After the dropwise addition of acetic acid (1.5 mL), the solution was ultrasonicated for 5 min and transferred to a Teflon-lined stainless steel autoclave (capacity 40 mL) to reach an 80% filling height. The reaction was performed at 180 °C for 2 h. The brick red powder was then collected, washed several times with deionized water and ethanol, and dried at 60 °C for 12 h. This catalyst was used for the preparation of various composite samples by wet impregnation.

Ex situ synthesis of Cu^0/Cu_2O: In a typical procedure described elsewhere,[24] 0.4 g of NaOH was added to 100 mL of 0.1 M $Cu(NO_3)_2{\cdot}3H_2O$ under magnetic stirring. After the complete dissolution of NaOH, 2 g of ascorbic acid was added, and the resulting mixture was stirred for 30 min at room temperature. During the process, the solution changed from blue to brown. The precipitate formed was then washed several times with water and ethanol and finally dried overnight at 60 °C.

Synthesis of Nb_2O_5: The Nb_2O_5 was synthesized using the hydrothermal procedure described elsewhere.[25] In a typical synthesis route, ammonium niobate(V) oxalate hydrate (Sigma-Aldrich, $C_4H_4NNbO_9{\cdot}H_2O$, 99.99%) (9.0894 g, 30 mmol) was dissolved in 200 mL of deionized water. Following 1 h of vigorous stirring, the pellucid solution was sealed in a Teflon-lined stainless steel autoclave and heated for 24 h at 175 °C. The solid formed during the hydrothermal treatment was then separated by filtration, washed with deionized water, dried at room temperature, and calcined for 4 h at 450 °C.

For all composites, the given powders with the desired proportions are ground and manually mixed in a mortar for a few minutes before making pellets for the photocatalytic tests. Each sample has been subjected to duplicate preparations and, in the case of the most active samples, triplicate preparations, followed

https://doi.org/10.1021/acscatal.3c04690
ACS Catal. 2023, 13, 16266−16278

by subsequent testing to evaluate the errors associated with both samples' preparation and experimentation.

2.3. Characterization. X-ray powder diffraction (XRPD) analyses of all materials were carried out with a PANalyticalX'-Pert Pro diffractometer with Cu Kα irradiation (λ = 1.5418 Å). The XRPD diagrams were recorded at room temperature between 3 and 90° (2θ) with a step size of ∼0.014°. Phase identifications were performed with the PANalytical High Score Plus program. The XRPD patterns (Figure S1) correspond to the expected ones for all the metal oxides used in this study. The Scherrer equation ($D = k\lambda/\beta \cos\theta$) was employed to compute the crystal's average size of both Cu_2O and Cu^0 particles. Nitrogen adsorption/desorption measurements were performed with an ASAP 2020 MP instrument. The specific surface areas of the metal oxides were calculated using the Brunauer-Emmett-Teller (BET) equation. The pore volume and pore diameter were determined by the Barrett−Joyner−Halenda (BJH) and density functional theory (DFT) methods, respectively. Before the measurements, samples were *in situ* outgassed at 300 °C for 3 h.

Diffuse reflectance (DR) UV−vis measurements were used to estimate the band gap of the semiconductors using a Cary 4000 UV−vis spectrophotometer and a Harrick praying mantis diffuse reflectance accessory. All spectra were recorded between 200 and 800 nm using an average time of 0.2 s and a scan rate of 300 nm/min. The positions of the conduction band (CB) and valence band (VB) of all photocatalysts were computed using the atom's Mulliken electronegativity equations[26]

$$E_{VB} = X - E_e + 12E_g \quad (1)$$

$$E_{CB} = E_{VB} - E_g \quad (2)$$

where E_{VB} is the VB potential, E_{CB} is the CB potential, E_e is the energy of free electrons on the hydrogen scale (ca. 4.5 eV), E_g is the band gap energy estimated from DR UV−vis measurements (Figure S2), and X is the absolute electronegativity of the semiconductor. The positions of CB and VB of the metal oxides used are represented in Scheme S1.

Transmission electron microscopy (TEM), including high-resolution TEM (HRTEM), electron diffraction (ED), and energy-dispersive X-ray (EDX) scanning TEM (STEM) elemental mapping, was carried out on a cold field-emission gun JEOL 200F microscope operated at 200 kV equipped with an EDX detector JEOL Centurion XL.

Both electrochemical and photoelectrochemical experiments were performed by using a potentiostat Autolab PGSTAT302N in a two-compartment cell and three-electrode configuration. The cathodic compartment was physically separated from the anodic one by a proton exchange membrane (Nafion 117; thickness 0.007 in). The fluorine-doped tin oxide-covered glass (FTO) was utilized as a conductive substrate for the working electrode (geometric area 0.71 cm^2), Pt wire was applied as counter electrode, and mercury sulfate electrode (Hg/Hg_2SO_4/sat. K_2SO_4) was the reference electrode. The aqueous electrolyte solutions used were 0.1 mol·dm^{-3} Na_2SO_4 at pH = 6.4 after saturation in argon. The electrochemical experiments were performed at different scan rates of 50, 100, and 150 mV·s^{-1}. Catalyst solutions were prepared by suspending 10 mg of photocatalyst in a mixture of 200 μL of Nafion solution (0.5 wt %) and 20 μL of ethanol followed by sonification for 30 min. Thereafter, 20 μL of the sample solution was pipetted onto the FTO surface (geometric area 0.71 cm^2) followed by drying at 80 °C for 10 min. For photoelectrochemical experiments, the light-emitting diode (LED) at λ = 405 nm was used as a light source. The photocurrent vs time curves were measured at the imposed potential of 0.5 V vs saturated calomel electrode (SCE) under chopped light.

2.4. Photocatalytic Tests. A sandwich-like cell reactor was used to study the performance of the different samples during the photodecomposition of formic acid under visible irradiation at room temperature (RT = 25 °C), as detailed in refs 27 and 28 and in Scheme S2. All experiments were performed in the vapor phase (2600 ppm of formic acid in argon) under continuous flow with a total flow rate of 25 cc·min^{-1}. Due to the difficulties in preparing a self-supported pellet of some composites, all metal oxides were mixed with the inert SiO_2 (SiO_2 content in the composite = 50 wt %) to make a pellet of ∼20 mg with a thickness of around 65 μm. Then, the catalyst was activated under Ar at RT under visible irradiation using a Xe lamp (LC8 Hamamatsu, 75 mW/cm^2 of irradiance) with a pass-high filter >390 nm. The relative concentrations of the effluent gas were stabilized before being sent to the cell, then an adsorption step of formic acid on the catalyst surface was performed in dark before turning on the lamp. Finally, the catalyst surface as well as the composition of the output gas from the reactor were simultaneously analyzed by an IR spectrometer (ThermoNicolet NEXUS 670 FTIR) equipped with a mercury cadmium telluride (MCT) detector with a spectral resolution of 4 cm^{-1} and accumulating 64 scans. Mass spectrometry (MS, Quadrupole Pfeiffer Omnistar GSD 301) was also used to monitor the gas composition during the reaction. The concentration of FAc in the gas phase was calculated using the surface area of the IR band at 1109−1101 cm^{-1} and the MS signals at m/z = 45 and 46. The CO_2 and CO selectivities were determined by using the IR band area at 2395−2182 cm^{-1} and 2140−2020 cm^{-1}, respectively. The amounts of hydrogen were determined by its MS signal at m/z = 2 after correction from water contributions and confirmed by an online gas chromatography (GC) analysis (see examples in Figure S3).

The formic acid conversion (expressed in% or mmol per hour per g of photocatalyst per irradiated surface) and the selectivity (%) were calculated from eqs 3−6 at the steady state using the calibration curve for different products of the reaction. The apparent quantum yield was calculated using the actinometer method, as detailed in the Supporting Information (Figure S4). The irradiated surface of the pellet is about 1.6 cm^2 (∼20% of the 2 cm^2 total surface is not irradiated due to the metallic holder shadow effect).

$$\text{FAc conversion (\%)} = \frac{[\text{FAc}]_0(\text{ppm}) - [\text{FAc}]_t(\text{ppm})}{[\text{FA}]_0(\text{ppm})} \times 100 \quad (3)$$

$$\begin{aligned}\text{Conversion rate}(\text{mmol}\cdot\text{h}^{-1}\cdot\text{g}^{-1}) &= \{\text{Total flow}(\text{L}\cdot\text{h}^{-1}) \times [\text{FAc}]0(\text{ppm}) \times 10^{-6} \\ &\times \frac{\text{conversion \%}}{100} \times 1000\} \\ &/[M_{\text{FAc}}(\text{g}\cdot\text{mol}^{-1}) \times \frac{1}{d_{\text{FAc}}}(\text{L}\cdot\text{g}^{-1}) \times m_{\text{catalyst}}(\text{g})]\end{aligned} \quad (4)$$

$$\text{Conversion in } \mu\text{mol}\cdot\text{h}^{-1}\cdot\text{cm}^{-2} = \frac{\text{Conversion rate}(\mu\text{mol}\cdot\text{h}^{-1}\cdot\text{g}^{-1}) \times m_{\text{catalyst(g)}}}{S_{\text{irradiated}}(\text{cm}^2)} \quad (5)$$

https://doi.org/10.1021/acscatal.3c04690
ACS Catal. 2023, 13, 16266−16278

Table 1. Results of the Formic Acid Reforming and the Corresponding Products at the Steady State (during 17 h of Reaction) over the Various Catalysts[a]

Samples	Conversion %[b]	Conversion rate[c]	H_2[c]	CO_2[c]	CO[c]	H_2/CO_2 selectivity (%)	Φ_{H2} (%)[e]	Induction time (h)[d]
Cu_2O	5.6	6.5 (1.05)	0.66	0.63	0	>99	1.38	3.6
Cu_2O/CuO	7.8	8.7 (1.40)	0.83	0.88	0	>99	1.48	1.6
Cu_2O/CeO_2	12.7	14.2 (2.28)	1.35	1.39	0.07	95	2.41	0.5
Cu_2O/Fe_2O_3	15.1	18.1 (2.91)	1.65	1.79	0.06	96	2.94	1.1
$Cu_2O/Cu-Fe-O$	19.7	21.7 (3.48)	2.05	2.24	n.d.	≈99	3.64	0.5
Cu_2O/TiO_2	25.8	28.8 (4.62)	0.84	1.01	2.02	34	1.49	0.7
Cu_2O/Nb_2O_5	30.0	36.0 (5.77)	1.12	1.36	2.53	36	1.98	0.8
Cu_2O/Fe_3O_4	55.0	61.8 (9.89)	5.65	6.15	0	>99	10.02	0.7

[a]Reaction conditions: [FAc] = 2600 ppm (0.26%) in Ar; total flow 25 $cm^3 \cdot min^{-1}$; T = 25 °C; Xe lamp 150 W with visible light pass filter (λ > 390 nm); irradiance = 71 $mW \cdot cm^{-2}$; m_{cat} = 10 mg (self-supported pellet with surface of 1.6 cm^2). [b]Error on the conversion is ±5%. [c]In $\mu mol \cdot h^{-1} \cdot cm^{-2}$ ($mmol \cdot g^{-1} \cdot h^{-1}$). n.d. stands for nondetected (under the detection limit of the apparatus). [d]Corresponds to the delay between the irradiation time and the time to reach a plateau (steady state). [e]Apparent quantum yield%.

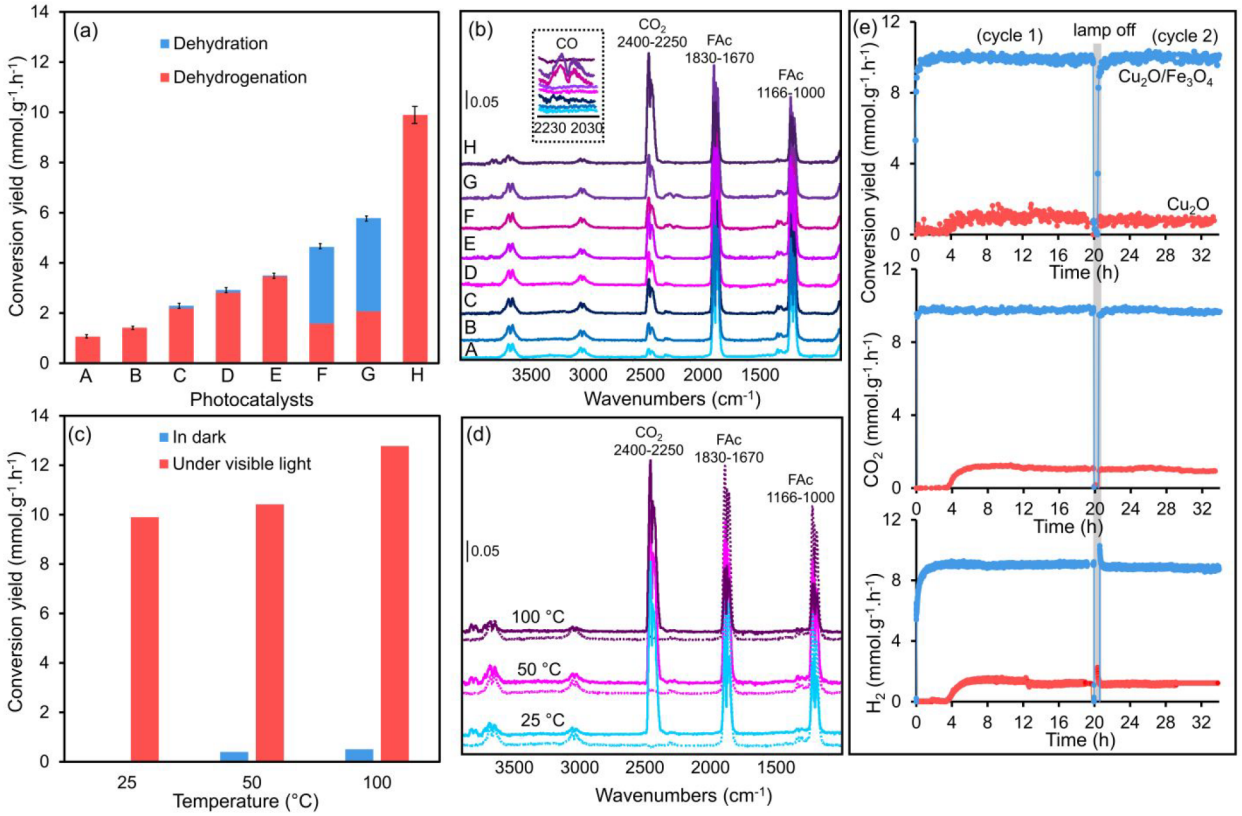

Figure 1. (a) FAc conversion rate and selectivity at steady state. (b) FTIR gas spectrum at steady state over (A) Cu_2O as monocomponent and bicomponent with (B) CuO, (C) CeO_2, (D) Fe_2O_3, (E) Cu−Fe−O spinel, (F) TiO_2, (G) Nb_2O_5, and (H) Fe_3O_4 under visible irradiation at RT. Inset: zoom on the CO FTIR region (2230−2050 cm^{-1}). (c) Effect of the temperature on FAc conversion over Cu_2O/Fe_3O_4 and (d) the corresponding FTIR spectra of the reaction gas phase at steady state, in the dark (dashed line), and under visible light (solid line). (e) Evolution of the conversion rate and the corresponding gas-phase products CO_2 and H_2 during FAc photoreforming over Cu_2O and Cu_2O/Fe_3O_4 during two cycles ((1) and (2)) under visible irradiation at RT.

$$\text{Selectivity}(\%) = \frac{\text{Concentration of target product(ppm)}}{\text{Concentration of FAc converted(ppm)}} \times 100 \text{ with target product} = H_2/CO_2 \text{or CO} \quad (6)$$

2.5. Ab Initio Calculations. Based on our experimental findings as well as related literature,[29−32] our calculations were performed to model the catalytic reaction on Fe_3O_4-(111), Cu-(100), and Cu_2O-(110) surfaces as well as on Cu^0(100)/Cu_2O(110) interface models. All these slab models are at least five atomic layer thickness, where the top three atomic layers are fully relaxed during the structural optimization at the density functional theory (DFT) level and the remaining atomic layers were fixed to mimic the bulk phase. These DFT calculations were performed with the generalized gradient approximation (GGA) of Perdew−Burke−Ernzerhof (PBE) functional[33] as implemented in the Vienna *Ab initio* Simulation Package (version 5.4.4).[34] Regarding the Fe-based surfaces, the PBE functional was combined with a Hubbard correction and an effective U value of 5.3 eV was applied to account for the strong correlation of an unfilled d orbital of Fe atoms, in accordance with previous studies.[35,36] The plane wave energy cutoff was set to 520 eV with an energy precision of 10^{-5} eV, and atomic

https://doi.org/10.1021/acscatal.3c04690
ACS Catal. 2023, 13, 16266−16278

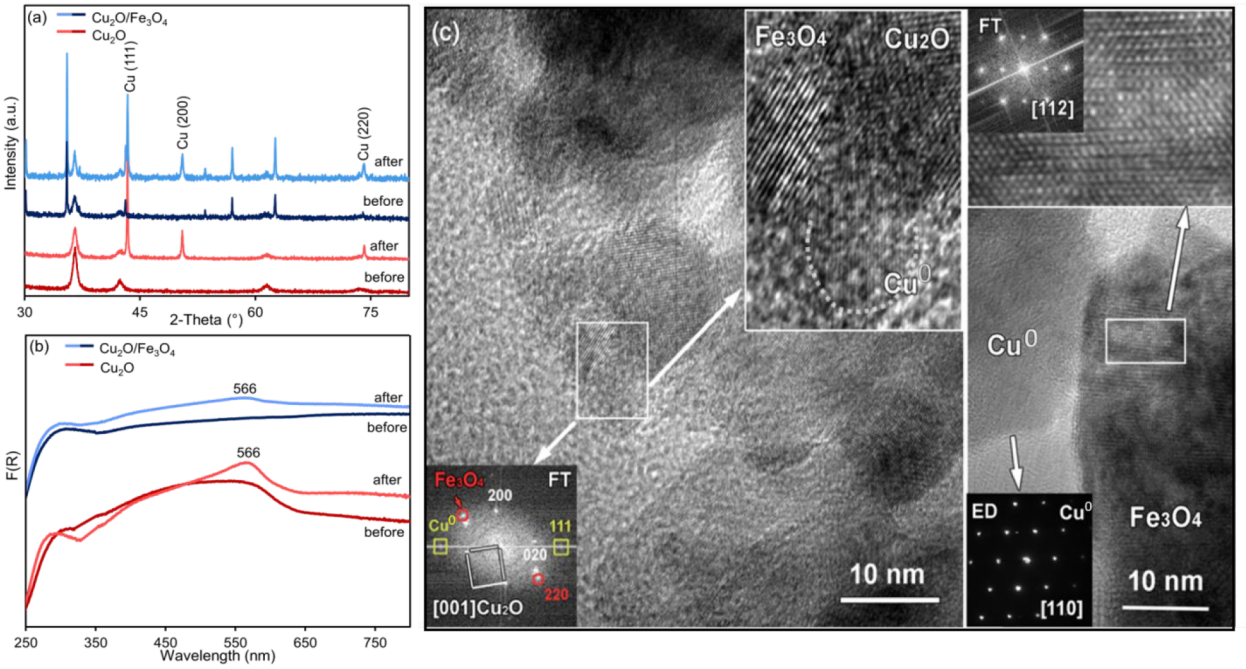

Figure 2. (a) XRPD patterns, and (b) DR-UV−vis spectra of Cu_2O and Cu_2O/Fe_3O_4 before and after the photoreforming of FAc reaction. (c) High-resolution bright-field TEM images of Cu_2O/Fe_3O_4 sample after reaction. The insets in the upper left corners show magnified high-resolution images selected by white boxes in the left and right panels. The corresponding FT patterns indexed based on the cubic Cu_2O, Cu, and Fe_3O_4 structures and the ED pattern indexed based on Cu^0 [110] are given as insets.

positions were relaxed until the maximum force on each atom was less than 1×10^{-3} eV per Å. To sample the Brillouin zone, a $2 \times 2 \times 1$ Monkhorst−Pack k-mesh grid was used for all slab models.[37] Periodic boundary conditions were used in all directions. Gaussian smearing with a width of 0.05 eV was utilized to aid in convergence of the DFT calculations. Long-range interactions were accounted for using the DFT-D3 method of the Grimme van der Waals correction.[38] Zero-point energy corrections were thus calculated for HCOOH(g), $CO_2(g)$, $H_2(g)$, HCOOH*, HCOO*, COOH*, and H* by assuming a quantum harmonic oscillator possessing the calculated vibrational frequencies.

3. RESULTS AND DISCUSSION

3.1. Photocatalytic Activity of Cu_2O/M_xO_y Composites.

Effect of the nature of the metal oxide: H_2 production through the photocatalytic decomposition of HCOOH was first performed in the presence of Cu_2O as a monocomponent and combined with different metal oxides such as CuO, CeO_2, Fe_2O_3, Cu−Fe−O spinel, Nb_2O_5, TiO_2, and Fe_3O_4. The components in the composites were mixed uniformly to maximize the interface between Cu_2O and selected metal oxide, and each experiment was repeated at least three times to minimize the relative errors (estimated to be around 5%). The FAc conversion rate (expressed in %, $\mu mol \cdot h^{-1} \cdot cm^{-1}$, and $mmol \cdot g^{-1} \cdot h^{-1}$ where g corresponds to the mass of the catalyst and cm^{-2} corresponds to the irradiated surface), as well as the produced amount of H_2, CO_2, and CO and their corresponding selectivity over various systems, are summarized in Table 1 and assembled in Figure 1a. For all systems, the molar conversion rates of FAc are almost equal to the sum of CO_2 (or H_2) and CO, demonstrating the absence of other carbon beside products.

Experiments on metal oxides used as monocomponent, such as CuO, CeO_2, Fe_2O_3, Cu−Fe−O spinel, Nb_2O_5, TiO_2, and Fe_3O_4, showed very low H_2 production (<5% of FAc conversion) under visible light (Table S2). These results can be explained either by the unsuitable conduction band (CB) position of some metal oxides situated below the reduction potential of H^+/H_2 (−0.18 V) or by the wide band gap (E_g) of others (i.e., Nb_2O_5 and TiO_2) that are only *active in the UV region* (see Scheme S1). Despite the good visible light absorption of Cu_2O, the photocatalyst shows poor activity (5.6% of FAc conversion) during the reaction despite the suitable position of its conduction band (CB ≈ −1.09 V) as compared to the reduction potential of the H^+/H_2 pair (−0.18 V) (Scheme S1). This might be related to the narrow band gap of Cu_2O (E_g = 1.98 eV) resulting in a high electron−hole recombination rate.[39] Interestingly, a synergetic effect is observed for the Cu_2O/Fe_3O_4 composite with 55% FAc conversion and 9.89 $mmol \cdot g^{-1} \cdot h^{-1}$ H_2 production rate at steady state, with an apparent quantum yield (Φ_{H2}) of 10% (Table 1) without any significant deactivation for 17 h of reaction (Figure 1e). This is the highest H_2 production rate compared to the other composites studied here ($Cu_2O/Fe_3O_4 \gg Cu_2O/Nb_2O_5 > Cu_2O/TiO_2 > Cu_2O/Fe_2O_3 \approx Cu_2O/CeO_2$) and to most of the Cu-based systems investigated in the literature (Table S3). The superior photocatalytic activity of Cu_2O/Fe_3O_4 is not directly dependent on the surface areas of the semiconductors since Fe_3O_4 exhibits the lowest surface area (6 m^2/g, Table S1) compared to the other semiconductors used in this study (i.e., Nb_2O_5, TiO_2, CeO_2, Table S1). Thus, the surface area of the semiconductor cannot be regarded as the determining factor affecting the exceptional photocatalytic activity of Cu_2O/Fe_3O_4. Moreover, and contrary to other composites, Cu_2O/Fe_3O_4 shows a total selectivity toward dehydrogenation since no CO is detected in the outlet gas (Table 1, Figure 1a,b). Thus, the nature of the metal oxide affects not only the photocatalytic activity but also the selectivity of the reaction, noting that CO production does not occur on Cu_2O, which is characterized by a high selectivity toward dehydrogenation. The lowest dehydrogenation selectivity (34−

https://doi.org/10.1021/acscatal.3c04690
ACS Catal. 2023, 13, 16266−16278

36%) is observed over Cu_2O combined with UV-photoactive catalysts such as TiO_2 and Nb_2O_5. In both systems, only the electrons of Cu_2O can be excited under visible light (with a cutoff filter at $\lambda > 390$ nm) to the conduction band and then moved to the CB of TiO_2 or Nb_2O_5. This leads to a better separation of electron and hole pairs within the Cu_2O matrix but less efficient H_2 production. This is because dehydration (CO + H_2O formation) is the favored pathway over these composites probably due to the surface acidity of both Nb_2O_5 and TiO_2.[40−42]

Effect of the temperature: Besides the nature of the metal oxides, the effect of the reaction temperature on the photocatalytic performance of highly active Cu_2O/Fe_3O_4 was also investigated (Figure 1c,d). No significant thermoactivity is observed in the dark below 100 °C (Figure 1c). However, increasing the temperature enhances the photocatalytic activity without any effect on the selectivity since only CO_2 and H_2 have been detected at the different temperatures (Figure 1d). Consequently, the reaction is mainly photocatalytic rather than thermal.

3.2. In Situ Restructuring of Copper Species during the Reaction over Cu_2O/Fe_3O_4. Based on the previous results, the Cu_2O/Fe_3O_4 composite, with the highest photocatalytic activity, is chosen to be studied in depth during the photoreforming of formic acid. The evolution of FAc conversion rate and CO_2 and H_2 production is compared to Cu_2O during two consecutive cycles (17 h/cycle) (Figure 1e). In the first cycle, the reaction over Cu_2O starting only after 3.6 h of visible irradiation can be defined as the induction period of the reaction. The CO_2 and H_2 follow instantly the HCOOH conversion over Cu_2O. This induction period becomes much shorter (<1 h) when Cu_2O is mixed with Fe_3O_4. A similar induction period is also observed for the other composites, except for Cu_2O/Fe_2O_3 showing a longer induction time (>1.6 h, Table 1, Figure S5). However, no significant induction period is observed in the second cycle over the Cu_2O and Cu_2O/Fe_3O_4 photocatalysts, suggesting that the active sites are already structured during the first cycle (Figure 1e). Both photocatalysts are ultrastable under visible irradiation with no deactivation observed at the prolonged period of 30 h with a constant FAc conversion and a total CO_2/H_2 selectivity. Such behavior was already observed in our previous work and assigned to the restructuring of $Cu^{(I)}$ into the $Cu^{(0)}/Cu^{(I)}$ binary system.[43,44]

To confirm the *in situ* formation of Cu^0, both Cu_2O and Cu_2O/Fe_3O_4 were *ex situ* characterized before and after the reaction by XRPD and DR-UV−vis (Figure 2a,b). The characteristic diffraction peaks of Cu^0 located at 43.7°, 50.7°, and 74.3° corresponding to the (111), (200), and (220) planes are observed in both samples after the reaction (Figure 2a).[45] Furthermore, the DR-UV−vis spectra show a single surface plasmon resonance (SPR) peak at 566 nm, which indicates the formation of metallic copper sites (Figure 2b).[46] Additional TEM analysis was performed on Cu_2O/Fe_3O_4 composites after the reaction to gain insight into the environment of copper (Figures S6 and 2c). The EDX-STEM elemental mapping of the Cu_2O/Fe_3O_4 sample after reaction (Figure S6) reveals the presence of Cu regions (in red in overlaid color map) along with Cu_2O (in pink in the overlaid color map as a mixture of Cu-red and O-blue). Further observations by HRTEM and EDX measurements confirm the coexistence of Cu^0 and Cu_2O thanks to the expected lattice spacing (Figure 2c, FT pattern Cu-yellow, Cu_2O-white, Fe_3O_4-red). In addition, the [112] Fe_3O_4 was seen in the interface with the copper particles to form the ternary $Cu^0/Cu_2O/Fe_3O_4$ system after the reaction. It is worth noting that we were not able to detect the Cu^0 by *ex situ* X-ray photoelectron spectroscopy (XPS) due to the reoxidation of the catalyst surface into Cu^{2+} when the catalyst is exposed to the atmosphere (the results are not shown here for the sake of brevity).

The above results suggest the *in situ* restructuring of Cu_2O into a binary system of Cu_2O/Cu^0 upon visible light irradiation and in the presence of FAc, in agreement with the literature.[43,44] It is worth noting that the mean particle size of the *in situ* formed Cu^0, as calculated by Scherrer equation, is larger than that of Cu_2O in both Cu_2O and Cu_2O/Fe_3O_4 samples after reaction (ca. 18 vs 49 or 73 nm, respectively; see Table S4). This is mainly due to the potential sintering of Cu^0 nanoparticles and clusters into larger particles under the reaction conditions (visible irradiation, continuous exposure to formic acid vapor), which is not the case of the oxides such as Cu_2O.[47] A similar phenomenon has been previously documented during methanol photo-oxidation over highly dispersed silver (Ag) embedded into ZX-Bi zeolite where the migration and aggregation of sub-nanosized $Ag_n^{\delta+}$ clusters resulted in the formation of larger Ag nanoparticles with the evolution of reaction time.[28] However, the TEM analysis demonstrates a polydispersity of the Cu^0 particle size with the presence of clusters at the interface of Cu_2O and Fe_3O_4 (Figure 2c). The important role of the Cu^0 particles in the photocatalytic process is confirmed by testing under similar reaction conditions an additional Cu_2O/Cu^0 sample, *ex situ* prepared as detailed in the Experimental Section. Higher activity (48% vs 6%) and a much shorter induction period are observed for the *ex situ* prepared Cu_2O/Cu^0 with respect to Cu_2O (Figure S7), which confirms that the induction period is related to the restructuring of Cu_2O into Cu_2O/Cu^0. However, performing a direct comparison in terms of photocatalytic activity between Cu_2O-based samples and the *ex situ* prepared Cu_2O/Cu^0 is not equitable. This is due to the fact of uncontrollable *in situ* formation of Cu^0 in the Cu_2O-based samples, leading to a final composition (Cu_2O/Cu^0 molar ratio, particle size, dispersion, etc.) that differs from the *ex situ* prepared Cu_2O/Cu^0. As a result, the two materials cannot be considered equivalent for a direct comparison in terms of their photocatalytic activities, and the use of Cu_2O/Cu^0 as additional reference material is to highlight the *in situ* restructuring phenomena observed over Cu_2O under working conditions. On the other hand, the major disadvantage associated with the *ex situ* synthesis of Cu_2O/Cu^0 is *its low stability where* Cu^0 species undergo oxidation with time under ambient conditions (in the presence of humidity) and a significant loss of activity has been observed with the time in respect to the fresh sample (Figure S8). Thus, the *in situ* formation of Cu^0 over the highly stable Cu_2O/Fe_3O_4 catalyst is therefore more advantageous as it can be stored under ambient condition.

On the other hand, it is important to note that we did not observe a similar reduction of Fe^{II}/Fe^{III} to Fe^0 and the formation of corresponding metal clusters in the Cu_2O/Fe_3O_4 sample. This absence of reduction is supported by our examination of XRD patterns (no characteristic peak at 47°) and HRTEM imaging.

3.3. Z-Scheme Mechanism over Cu_2O/Fe_3O_4. In contrast to Fe_2O_3, which displayed negligible activity, Fe_3O_4 exhibited some catalytic activity. However, the key observation is that the synergistic effect we reported is evident only when Cu_2O and Fe_3O_4 are combined. Various factors can be posited to elucidate the origin of the synergetic effect observed when employing

https://doi.org/10.1021/acscatal.3c04690
ACS Catal. 2023, 13, 16266−16278

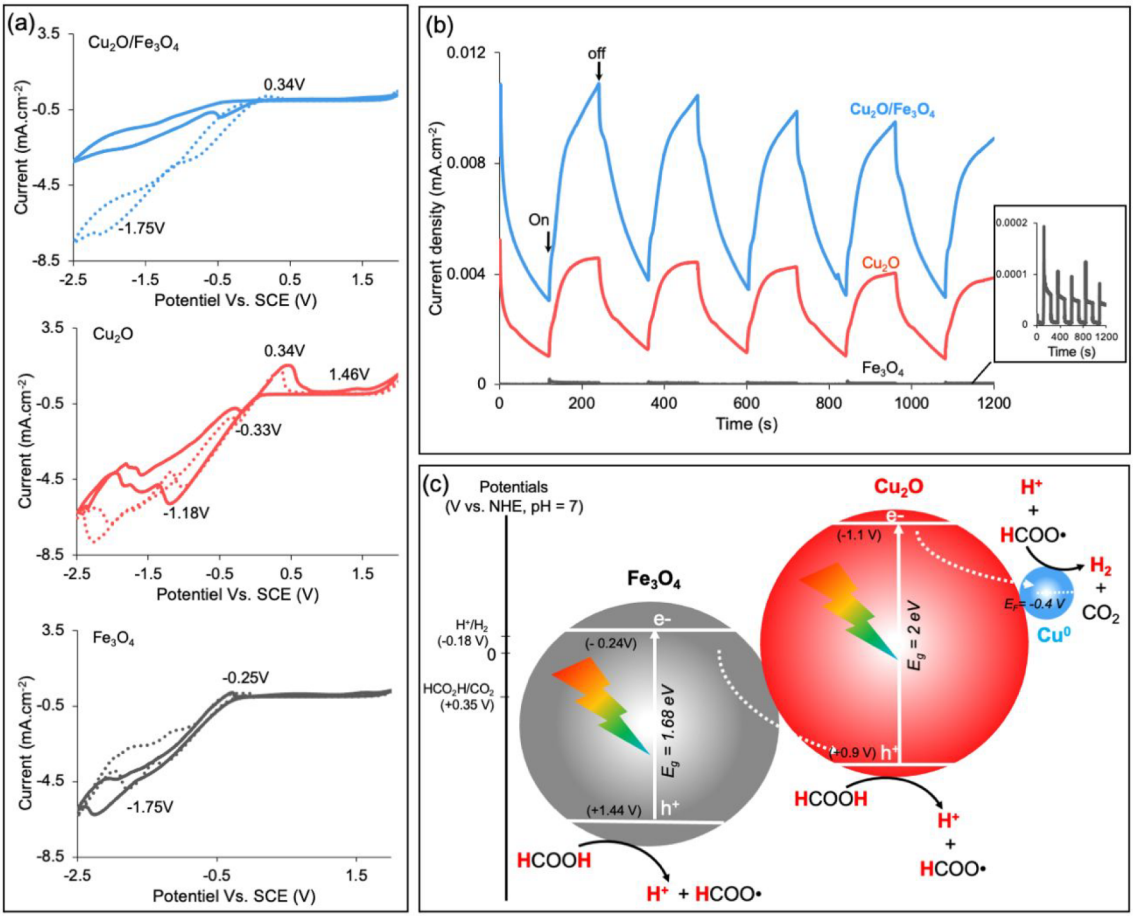

Figure 3. (a) CV response of Cu_2O, Fe_3O_4, and Cu_2O/Fe_3O_4 electrode before (dashed curve) and after visible light irradiation (solid curve). Electrolyte, 0.1 mol·dm^{-3} Na_2SO_4. Scan rate: 50 mV·s^{-1}. (b) Plots of photocurrent vs time recorded for all photocathodes in 0.1 mol·dm^{-3} sodium sulfate electrolyte saturated with argon at a potential of 0.5 V. The pulsed responses were recorded upon illumination with visible light. Inset: zoom in on the photoresponse of Fe_3O_4. (c) Schematic diagram showing the photoinduced charge-carriers transfer and the H_2 production through the photodecomposition of formic acid under visible light over Cu_2O/Fe_3O_4 composite.

magnetite (Fe_3O_4) as a cophotocatalyst in comparison to hematite (Fe_2O_3). These factors comprise the positions of the conduction band (CB) and valence band (VB) (Scheme S1), the narrower band gap exhibited by Fe_3O_4, and the lower effective mass of photoinduced electrons in the case of hematite (3.98me compared to 16.4me for Fe_2O_3).[48,49] It is important to note that the effective mass of electrons may exhibit variation contingent upon specific conditions (particle size, crystallinity, defects, etc.) and the electronic band structures of the materials. Nonetheless, the discrepancy in effective mass is substantial, differing by several orders of magnitude, and plausibly justifies the shorter induction time observed in the case of Cu_2O/Fe_3O_4. This can be attributed to a more efficient and rapid transfer of the photoinduced electron from Fe_3O_4 to Cu_2O.

Therefore, the photoelectrochemical behavior of the Cu_2O/Fe_3O_4 binary composite was investigated to better understand its performance. Cu_2O and Fe_3O_4 were used as monocomponent catalysts for comparison. The cyclic voltammetry (CV) response of Fe_3O_4 (Figure 3a), investigated in 0.1 M sodium sulfate solution at the potential window of −2.5 V; 2.5 V vs SCE, shows the oxidation and reduction peaks of iron species contained in Fe_3O_4 as previously reported in the literature.[50] Additional small humps (i.e., redox peaks) are also observed and can be related to the electrochemical reactions of sulfite anions adsorbed onto the surface of magnetite NPs.[51] As concerns Cu_2O, the oxidation of Cu_2O into CuO is observed at around +0.34 V vs SCE. In the reverse cycle a well-defined peak is observed at around −0.33 V vs SCE corresponding to the reduction of CuO into Cu_2O. Further reduction currents are most likely related to the formation of metallic copper.[52,53] The same redox peaks of Cu_2O and Fe_3O_4 are found in the cyclic voltammetry of the Cu_2O/Fe_3O_4 composite with a small shift (Figure 3a). On the other hand, there is no major change in the CV in the case of the Fe_3O_4 sample before and after visible irradiation, except to a shift of the reduction peak into negative potentials reflecting the facile transfer of the electrolyte into the electrode surface.[54] By contrast, changes are observed in the CV of Cu_2O but more significantly in that of Cu_2O/Fe_3O_4 under visible irradiation. The formation of new peaks in both samples under visible irradiation, in addition to the strong change in the current density of Cu_2O/Fe_3O_4 under visible irradiation, reveal the formation of new kinds of copper species confirming the possible *in situ* restructuring of Cu_2O under visible light. The transient photocurrent response tests under several on/off cycles of visible irradiation are illustrated in Figure 3b. The results indicate a higher photoresponse of Cu_2O/Fe_3O_4 with respect to both Cu_2O and Fe_3O_4. The slow rise of photocurrent response over both Cu_2O and Cu_2O/Fe_3O_4 is assigned to a low charge-carrier mobility.[55] The higher photocurrent density obtained over Cu_2O/Fe_3O_4 with respect to the monocompo-

https://doi.org/10.1021/acscatal.3c04690
ACS Catal. 2023, 13, 16266−16278

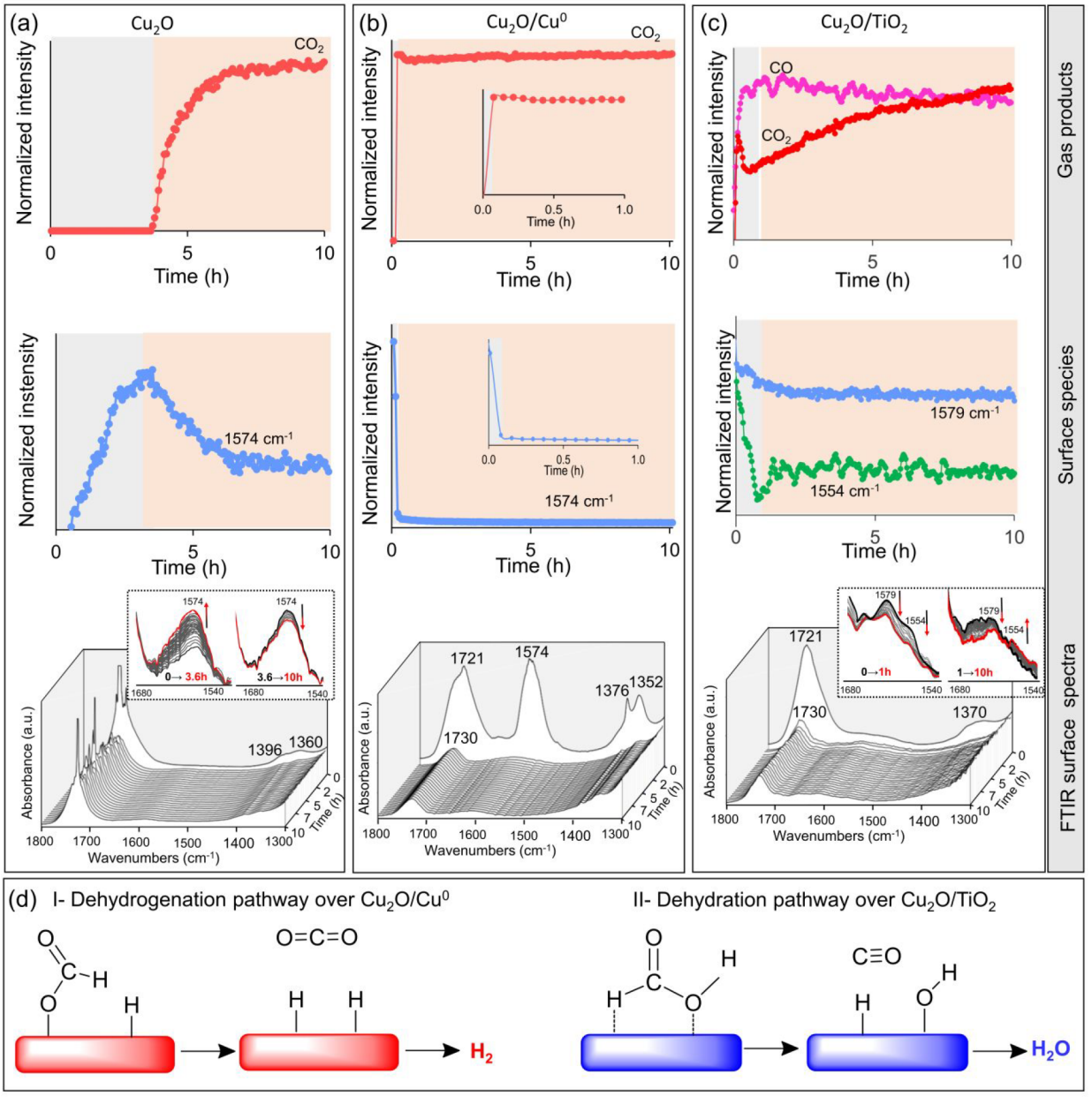

Figure 4. Evolution of CO_2 and CO gas products and surface formate species as well as the direct FTIR spectra of the photocatalyst surface during the photoreforming of FAc over (a) Cu_2O, (b) Cu_2O/Cu^0, and (c) Cu_2O/TiO_2. Only 1/5 of FTIR spectra are displayed here to increase visibility. Insets: zoom on some selected spectra in the 1500−1600 cm^{-1} FTIR region over Cu_2O in (a), zoom on the evolution of CO_2 and the formate species in the first hour of reaction over Cu_2O/Cu^0 in (b); zoom on some selected spectra in the 1500−1700 cm^{-1} FTIR region over Cu_2O/TiO_2 in (c). (d) Scheme of the dehydrogenation and dehydration pathways of HCOOH over Cu_2O/Cu^0 and Cu_2O/TiO_2, respectively.

nent samples, explained by an enhanced charge separation, is in agreement with the superior photocatalytic activity of this sample.

The H_2 generation through the photocatalytic decomposition of formic acid over the simple composite of Cu_2O and Fe_3O_4 can therefore proceed via two possible pathways: (i) double charge transfer mechanism (heterojunction of type II) or (ii) Z-scheme transfer. In the first pathway, the excited electrons from the VB of Fe_3O_4 and Cu_2O are transferred to their respective CB. The high CB position of Cu_2O and the interface with Fe_3O_4 may result in the transfer of electrons from Cu_2O to Fe_3O_4 and holes in the reverse direction. Therefore, effective separation of the photogenerated electrons and holes takes place at the interface, i.e., a net accumulation of e^- and h^+, respectively, on the CB of Fe_3O_4 and the VB of Cu_2O via a double charge transfer mechanism.[56] According to this pathway, the short induction period corresponding to the fast *in situ* restructuring of Cu_2O into Cu_2O/Cu^0 cannot be justified. Therefore, efficient H_2 production over Cu_2O/Fe_3O_4 favors the Z-scheme route as illustrated in Figure 3c. In this pathway, the CB electrons of Fe_3O_4 may recombine with the VB holes of Cu_2O. And thereby, a net accumulation of e^- and h^+ may occur on the CB of Cu_2O and the VB of Fe_3O_4, respectively, limiting the recombination process of the photogenerated charge carriers within Cu_2O or Fe_3O_4. The holes in Cu_2O are consumed by two competing routes, (i) combining with photoexcited electrons from Fe_3O_4 and (ii) reacting with formic acid to yield proton and formate. A maximum H_2 production can be achieved by a compromise

https://doi.org/10.1021/acscatal.3c04690
ACS Catal. 2023, 13, 16266−16278

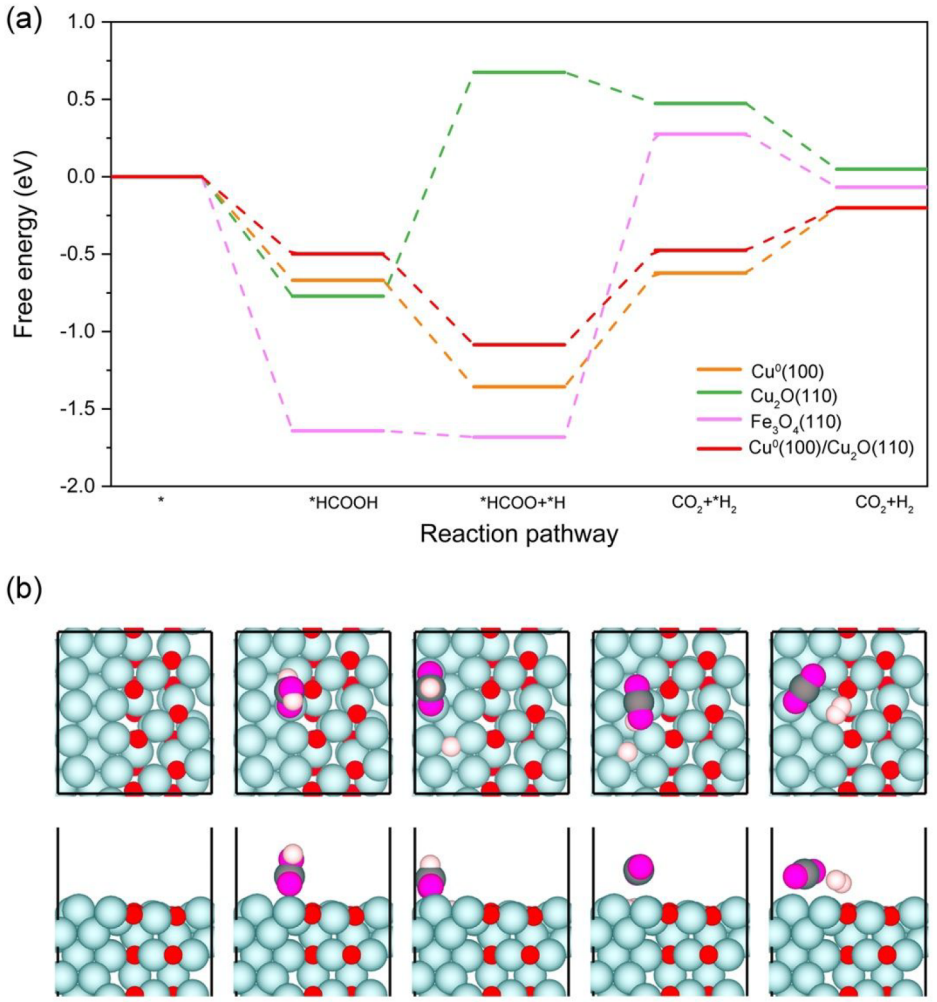

Figure 5. (a) DFT-Calculated Gibbs free energies for formic acid dehydrogenation reaction on the different explored metal surfaces and (b) corresponding DFT-derived structures of intermediates (Upper: top view; Bottom: side view) for $Cu^0(100)/Cu_2O(110)$. The total free energy of different models with a gas-phase HCOOH molecule was set as the zero point in the profile. The color code for FAc: O, pink; H, white; C, gray. The color scheme for $Cu^0(100)/Cu_2O(110)$ interface model: Cu, light-blue; O, red.

between these two pathways. Here, it seems that the recombination of h^+ from the VB of Cu_2O with e^- from the CB of Fe_3O_4 is the predominant route, and thus, the production of CO_2 and H_2 is spatially different: the oxidation of adsorbed formate into H^+ and CO_2 is mainly occurred on Fe_3O_4, while the photoexcited electrons accumulated on the CB of Cu_2O are involved in the *in situ* restructuring of Cu_2O (Figure 3c) into the binary Cu_2O/Cu^0 system.

To sum up, the highest photocatalytic activity of Cu_2O/Fe_3O_4 is explained by the efficient charge separation via the Z-scheme mechanism as well as the *in situ* restructuring of Cu_2O into a Cu_2O/Cu^0 binary system. The metallic copper (Cu^0) plays a key role on the collection of the photoinduced electrons to lower their overpotential for efficient H_2 production.[43]

3.4. Operando-FTIR Analysis. *Operando*-FTIR spectroscopy sheds light on the induction time as the evolution of the surface species is simultaneously monitored with the gas-phase analysis during the reaction. Unfortunately, we were not able to monitor the surface of the Cu_2O/Fe_3O_4 photocatalyst due to the depletion of IR transmittance through the pellet once the lamp is turned on, which is probably related to the multiphoton interband absorption, spectral hole burning, and carrier heating.[57,58] For this reason, Cu_2O (less active, highly selective), Cu_2O-Cu^0 (highly active, highly selective), and Cu_2O/TiO_2 (less active, less selective) were chosen to identify the reaction intermediates, to understand the origin of the induction period, the selectivity, and to propose a reaction mechanism. The experimental data recorded for SiO_2 used as an inert diluter are also shown for comparison. The attribution of different FTIR bands is summarized in Table S4.

The adsorption of FAc on the Cu_2O photocatalyst (Figure S9) leads to the formation of new bands at 1360, 1396, 1560, and 2947 cm^{-1}. Similar bands are observed on pure SiO_2 and attributed to weakly adsorbed FAc.[59] The formation of an intense band at 1721 cm^{-1} parallel to the decrease of the Si−OH and/or Cu(OH) band at 3735 cm^{-1} is associated with the C═O stretching mode of molecularly adsorbed FAc. Formic acid adsorbed on Cu_2O/Cu^0 gives additional bands at 1641 and 2888 cm^{-1} that are attributed to the $\nu_{as}(OCO)$ and $\upsilon(CH)$ stretching vibration of ligated HCOOH to the copper surface via the carbonyl bond. The intense maxima at 1574 and 1376 cm^{-1} are attributed to the adsorbed unidentate formate species on copper.[59] The band at 1355 cm^{-1}, probably overlapped with the physisorbed FAc, is due to copper formate. For TiO_2/Cu_2O, absorptions are seen at 1554 and 1370 cm^{-1} and assigned to $\upsilon_{as}(OCO)$ and $\upsilon_s(OCO)$ of bridged bidentate formate.[60]

https://doi.org/10.1021/acscatal.3c04690
ACS Catal. 2023, 13, 16266−16278

When the lamp is turned on, fast desorption of weakly adsorbed (1360−1395 and 1560 cm^{-1}) and physisorbed (1721 cm^{-1}) FAc is observed for all photocatalysts. For Cu_2O, the band at 1574 cm^{-1} gradually increases during the induction period without any production of CO_2 (Figure 4a), indicating the rearrangement of adsorbed formate on the photocatalyst surface. After 3 h of irradiation, a decrease in the band intensity of monodentate formate is observed, accompanied by the production of CO_2. In contrast, fast depletion of bands associated with formic acid ligated to copper metal sites (1640−2887 cm^{-1}) and unidentate formate (1376−1576 cm^{-1}) is observed over Cu_2O/Cu^0 accompanied by the production of CO_2 (Figure 4b). This confirms the decomposition of monodentate formate into aqueous CO_2 and H_2. Furthermore, the band at 1355 cm^{-1} also decreases because of the removal of physisorbed formic acid molecules, to reveal the presence of a maximum at 1356 cm^{-1} with a new band at 2853 cm^{-1} attributed to the bidentate copper formate. These species are almost stable and remain observed on the catalyst surface, even at a prolonged reaction time. For Cu_2O/TiO_2, the bands of bidentate formate (1554 cm^{-1}) are decreased upon irradiation accompanied by the production of CO with a higher amount than CO_2 at the beginning of the reaction (Figure 4c), while at a prolonged irradiation time, a decrease of the band located at 1579 cm^{-1}, attributed to monodentate formate, is observed accompanied by the production of CO_2 with a higher amount than CO (Figure 4c). Thus, the bidentate formate species adsorbed on TiO_2 are mainly decomposed into CO at the beginning of the reaction, while the monodentate species formed on the *in situ* restructured Cu_2O can rather be decomposed into CO_2. To resume, the HCOOH dehydrogenation over Cu_2O/Cu^0 proceeds by cleavage of the O−H bond to produce monodentate formate (HCOO*) and hydrogen (H*) on the surface (Figure 4d). The formate can break down further to form CO_2 and H*. The latter reacts with another surface H* to form H_2 in the gas phase. In the dehydration pathway, which mainly occurs over TiO_2, the HCO−OH bond of the bidentate species is cleaved into CO and H_2O.[41]

3.5. Complementary Microscopic Insight into the Reaction Mechanism by DFT Calculations. DFT calculations were performed to further explore the catalytic reaction mechanism. Based on the experimental findings on the Cu^0/Cu_2O system discussed above, the formic acid is expected to be preferentially decomposed via a dehydrogenation pathway ($HCOOH \rightarrow CO_2 + H_2$). Therefore, we focus here on this reaction pathway for a set of explored surfaces, e.g., Fe_3O_4-(111), Cu-(100), and Cu_2O-(110) surfaces as well as on $Cu^0(100)/Cu_2O(110)$.

The first step of the reaction implies the chemisorption of the HCOOH molecule on the exposed surface sites, as illustrated in Figure 5 for the $Cu^0(100)/Cu_2O(110)$ interface model as well as in Figures S10−S13 for the other surface slab models. Figure 5a reveals that the Gibbs free energy for the $HCOOH/Fe_3O_4$ species is much lower (−1.64 eV) compared to the other systems, indicating that the Fe_3O_4-(111) surface strongly adsorbs HCOOH, which would be detrimental to the subsequent steps of the catalytic mechanism, whereas the Cu-(100), Cu_2O-(110), and $Cu^0(100)/Cu_2O(110)$ interface models show moderate adsorption strengths. The next step of the reaction is then the cleavage of the O−H bond in *HCOOH, leading to the formation of adsorbed *HCOO. This elementary step of O−H bond cleavage is exothermic for Fe_3O_4-(111), $Cu^0(100)/Cu_2O(110)$ interface models but endothermic for Cu_2O-(110). To further explore the origin of this difference, we calculated the charge density difference of the *HCOO species adsorbed on the surfaces using the surface configurations of the Cu_2O-(110) and $Cu^0(100)/Cu_2O(110)$ interface model as an example. As shown in Figure S13, it is clear that the HCOO species adsorbed on the $Cu^0(100)/Cu_2O(110)$ interface model have more charge accumulation compared to the case of Cu_2O-(110) adsorption; therefore, this $Cu^0(100)/Cu_2O(110)$ interface scenario can remarkably stabilize the surface *HCOO species. At the same time, Bader charge transfer calculations[61] show a charge transfer of −0.88 *e* for the oxygen atom in HCOO species on the Cu_2O-(110) surface compared to −1.01 *e* for the $Cu^0(100)/Cu_2O(110)$ interface model, resulting in a stronger adsorption affinity for *HCOO species with the $Cu^0(100)/Cu_2O(110)$ model.

Once the O−H bond is broken, the remaining C−H bond in the formate (*HCOO) dissociates to form CO_2 and *H. Finally, the adsorbed H* intermediates are released from the surface sites and recombined to form a H_2 molecule. This is in accordance with the FTIR *operando* results. Throughout the reaction pathway, for Fe_3O_4-(111), $Cu^0(100)$, and $Cu^0(100)/Cu_2O(110)$ interface models, the rate-determining step (RDS) is the transition from HCOOH* + H* to CO_2 + 2H* with a corresponding free energy change (ΔG) of 1.96, 0.73, and 0.61 eV, respectively, while the C−H bond cleavage in adsorbed *HCOOH is the RDS for the Cu_2O-(110) surface model (ΔG = 1.45 eV). It can be observed that in the formation of the *HCOO step the Cu_2O-(110) and Fe_3O_4-(110) slab models exhibit different adsorption behaviors. This is mainly because Fe_3O_4-(110) shows a stronger adsorption ability for *HCOO than Cu_2O-(110), as shown in Figures S13 & S14. This trend is associated with a more pronounced charge transfer between the intermediate and the substrate for Fe_3O_4-(110) compared to Cu_2O-(110). For the subsequent step, the adsorption capability of Cu_2O-(110) is comparable to that of Fe_3O_4-(110 but weaker than that of Cu^0-(100) as revealed by Figure S14. This overall observation indicates that the $Cu^0(100)/Cu_2O(110)$ interface model shows the lowest energetic rate-determining step in line with the optimum catalytic activity observed experimentally.

4. CONCLUSIONS

The H_2 production via photoreforming of FAc is studied in the vapor phase under continuous flow over Cu_2O combined with other semiconducting metal oxide supports (CuO, CeO_2, Fe_2O_3, Cu−Fe−O spinel, Nb_2O_5, TiO_2, and Fe_3O_4) under visible light (λ > 390 nm) and at room temperature. It is shown that the reactivity and dehydrogenation selectivity of Cu_2O are strongly affected by the type of semiconductor. Among all semiconductors investigated in this work, the highest hydrogen conversion rate and apparent quantum yield are observed for the Earth-abundant Cu_2O/Fe_3O_4 composite (9.89 $mmol \cdot g^{-1} \cdot h^{-1}$; Φ_{H2} = 10%, respectively) with a total dehydrogenation selectivity (>99%) and high stability (>30 h). The enhanced reactivity of this catalyst originated from the efficient separation of the photogenerated charge carrier according to the Z-scheme mechanism. This charge separation process enabled fast and effective *in situ* restructuring of the Cu_2O-based composite under working conditions leading to the formation of metallic copper (Cu^0) as an active site for H_2 production. Results from mechanistic FTIR *operando* and DFT calculations reveal that the HCOOH dehydrogenation proceeds by cleavage of the O−H bond and the remaining C−H bond in the formate (*HCOO) dissociates to form CO_2 and *H. Finally, the adsorbed H*

https://doi.org/10.1021/acscatal.3c04690
ACS Catal. 2023, 13, 16266−16278

intermediates are released from the surface sites and recombined to form H_2 molecule.

■ ASSOCIATED CONTENT

Supporting Information

The Supporting Information is available free of charge at https://pubs.acs.org/doi/10.1021/acscatal.3c04690.

Extended experimental section, Textural properties of catalysts (Table S1), Activity and selectivity of reference materials (Table S2), Comparison of catalysts' activity and selectivity with results described in previous reports (Table S3), Mean particle size (Table S4), Assignment of IR bands (Table S5), XRD patterns of catalysts (Figure S1), DR UV−vis spectra of catalysts (Figure S2), GC chromatograms confirming formation of hydrogen over Cu_2O/CuO and $Cu_2O/Cu_{0.75}Fe_{2.25}O_4$ (Figure S3), UV−visible spectra of Fe-Phenanthroline solution (Figure S4), Evolution of conversion yield and the corresponding gas phase products (Figure S5), EDX-STEM elemental mappings of Cu_2O/Fe_3O_4 after reaction (Figure S6), Evolution of FAc conversion and the corresponding gas-phase products over Cu_2O and *ex-situ* prepared Cu_2O/Cu^0 under visible irradiation at RT (Figure S7), FAc conversion over fresh and aged Cu_2O/Cu^0 sample prepared *ex-situ* (Figure S8), IR spectra after FAc adsorption on selected catalysts (Figure S9), DFT-optimized different binding modes (Figures S10−S13), Diagram showing the CB and VB position of different semiconductors (Scheme S1), FTIR *Operando* setup and IR sandwich cell used in this study (Scheme S2) (PDF)

■ AUTHOR INFORMATION

Corresponding Authors

Mohamad El-Roz − *Laboratoire Catalyse et Spectrochimie, Normandie Université, ENSICAEN, UNICAEN, CNRS, 14050 Caen, France;* orcid.org/0000-0003-4450-211X; Email: mohamad.elroz@ensicaen.fr

Antoine Maignan − *Laboratoire CRISMAT, ENSICAEN, UNICAEN, CNRS, 14050 Caen, France;* orcid.org/0000-0002-4157-5367; Email: antoine.maignan@ensicaen.fr

Authors

Houeida Issa Hamoud − *Laboratoire Catalyse et Spectrochimie, Normandie Université, ENSICAEN, UNICAEN, CNRS, 14050 Caen, France;* orcid.org/0000-0003-4823-8395

Lukasz Wolski − *Laboratoire Catalyse et Spectrochimie, Normandie Université, ENSICAEN, UNICAEN, CNRS, 14050 Caen, France; Faculty of Chemistry, Adam Mickiewicz University, Poznań, 61-614 Poznań, Poland;* orcid.org/0000-0002-1207-0546

Hanen Abdelli − *Laboratoire Catalyse et Spectrochimie, Normandie Université, ENSICAEN, UNICAEN, CNRS, 14050 Caen, France; Research and Technology Centre of Energy (CRTEn), Laboratory of Nanomaterials and Systems for Renewable Energies (LaNSER), 2050 Hammam-Lif, Tunisia*

Radhouane Chtourou − *Research and Technology Centre of Energy (CRTEn), Laboratory of Nanomaterials and Systems for Renewable Energies (LaNSER), 2050 Hammam-Lif, Tunisia;* orcid.org/0000-0002-2878-0825

Oleg Lebedev − *Laboratoire CRISMAT, ENSICAEN, UNICAEN, CNRS, 14050 Caen, France*

Christine Martin − *Laboratoire CRISMAT, ENSICAEN, UNICAEN, CNRS, 14050 Caen, France;* orcid.org/0000-0003-1567-5505

Dong Fan − *Institut Charles Gerhardt Montpellier, 34095 Montpellier, France*

Guillaume Maurin − *Institut Charles Gerhardt Montpellier, 34095 Montpellier, France;* orcid.org/0000-0002-2096-0450

Complete contact information is available at: https://pubs.acs.org/10.1021/acscatal.3c04690

Author Contributions

The manuscript was written through contributions of all authors. All authors have given approval to the final version of the manuscript.

Notes

The authors declare no competing financial interest.

■ ACKNOWLEDGMENTS

The authors acknowledge the Normandy region (H_2CO_2 project) for the financial support. The authors acknowledge Jihan Dhainy for the electrochemical analysis and Juan Pablo Bolletta (CRISMAT) for interesting scientific discussions. L.W. gratefully acknowledges the National Science Centre, Poland (project no. 2018/28/C/ST5/00255) and the Polish Minister of Education and Science (decision no. SMN/16/0997/2020) for financial support. The computational work was performed using HPC resources from GENCI-CINES (Grant A0120907613).

■ REFERENCES

(1) Lakhera, S. K.; Rajan, A.; Rugma, T. P.; Bernaurdshaw, N. A Review on Particulate Photocatalytic Hydrogen Production System: Progress Made in Achieving High Energy Conversion Efficiency and Key Challenges Ahead. *Renew. Sustain. Energy Rev.* **2021**, *152*, 111694.

(2) Epron, F.; Duprez, D. Hydrogen Production by Catalytic Processes. In *Current Trends and Future Developments on (Bio-) Membranes;* Basile, A., Napporn, T. W., Eds.; Elsevier, 2020; pp 57−89. DOI: 10.1016/B978-0-12-817110-3.00003-5.

(3) Eppinger, J.; Huang, K.-W. Formic Acid as a Hydrogen Energy Carrier. *ACS Energy Lett.* **2017**, *2* (1), 188−195.

(4) Navlani-García, M.; Mori, K.; Kuwahara, Y.; Yamashita, H. Recent Strategies Targeting Efficient Hydrogen Production from Chemical Hydrogen Storage Materials over Carbon-Supported Catalysts. *NPG Asia Mater.* **2018**, *10* (4), 277−292.

(5) Kim, C.; Lee, K.; Yoo, I.-H.; Lee, Y.-J.; Ramadhani, S.; Sohn, H.; Nam, S. W.; Kim, J.; Kim, Y.; Jeong, H. Strategy for Efficient H_2 Production from a Mixture of Formic Acid and Formate Using Operando pH Measurements. *ACS Sustain. Chem. Eng.* **2022**, *10* (2), 888−898.

(6) Xu, R.; Lu, W.; Toan, S.; Zhou, Z.; Russell, C. K.; Sun, Z.; Sun, Z. Thermocatalytic Formic Acid Dehydrogenation: Recent Advances and Emerging Trends. *J. Mater. Chem. A* **2021**, *9* (43), 24241−24260.

(7) Navlani-García, M.; Salinas-Torres, D.; Mori, K.; Kuwahara, Y.; Yamashita, H. Photocatalytic Approaches for Hydrogen Production via Formic Acid Decomposition. *Top. Curr. Chem.* **2019**, *377* (5), 27.

(8) El-Roz, M.; Telegeiev, I.; Mordvinova, N. E.; Lebedev, O. I.; Barrier, N.; Behilil, A.; Zaarour, M.; Lakiss, L.; Valtchev, V. Uniform Generation of Sub-Nanometer Silver Clusters in Zeolite Cages Exhibiting High Photocatalytic Activity under Visible Light. *ACS Appl. Mater. Interfaces* **2018**, *10* (34), 28702−28708.

(9) Navlani-García, M.; Miguel-García, I.; Berenguer-Murcia, Á.; Lozano-Castelló, D.; Cazorla-Amorós, D.; Yamashita, H. Pd/Zeolite-

Based Catalysts for the Preferential CO Oxidation Reaction: Ion-Exchange, Si/Al and Structure Effect. *Catal. Sci. Technol.* **2016**, *6* (8), 2623−2632.
(10) Corredor, J.; Rivero, M. J.; Rangel, C. M.; Gloaguen, F.; Ortiz, I. Comprehensive Review and Future Perspectives on the Photocatalytic Hydrogen Production. *J. Chem. Technol. Biotechnol.* **2019**, *94* (10), 3049−3063.
(11) Yuan, Y.; Zhou, L.; Robatjazi, H.; Bao, J. L.; Zhou, J.; Bayles, A.; Yuan, L.; Lou, M.; Lou, M.; Khatiwada, S.; Carter, E. A.; Nordlander, P.; Halas, N. J. Earth-Abundant Photocatalyst for H_2 Generation from NH_3 with Light-Emitting Diode Illumination. *Science.* **2022**, *378* (6622), 889−893.
(12) Abdelli, H.; Hamoud, H. I.; Bolletta, J. P.; Paecklar, A.; Bardaoui, A.; Kostov, K. L.; Szaniawska, E.; Maignan, A.; Martin, C.; El-Roz, M. H_2 Production from Formic Acid over Highly Stable and Efficient Cu-Fe-O Spinel Based Photocatalysts under Flow, Visible-Light and at Room Temperature Conditions. *Appl. Mater. Today* **2023**, *31*, 101771.
(13) Kakuta, S.; Abe, T. A Novel Example of Molecular Hydrogen Generation from Formic Acid at Visible-Light-Responsive Photocatalyst. *ACS Appl. Mater. Interfaces* **2009**, *1* (12), 2707−2710.
(14) Koiki, B. A.; Arotiba, O. A. Cu_2O as an Emerging Semiconductor in Photocatalytic and Photoelectrocatalytic Treatment of Water Contaminated with Organic Substances: A Review. *RSC Adv.* **2020**, *10* (60), 36514−36525.
(15) Li, G.; Huang, J.; Chen, J.; Deng, Z.; Huang, Q.; Liu, Z.; Guo, W.; Cao, R. Highly Active Photocatalyst of Cu_2O/TiO_2 Octahedron for Hydrogen Generation. *ACS Omega* **2019**, *4* (2), 3392−3397.
(16) Pu, Y.; Luo, Y.; Wei, X.; Sun, J.; Li, L.; Zou, W.; Dong, L. Synergistic Effects of Cu_2O-Decorated CeO_2 on Photocatalytic CO_2 Reduction: Surface Lewis Acid/Base and Oxygen Defect. *Appl. Catal. B Environ.* **2019**, *254*, 580−586.
(17) Furukawa, S.; Tsukio, D.; Shishido, T.; Teramura, K.; Tanaka, T. Correlation between the Oxidation State of Copper and the Photocatalytic Activity of Cu/Nb_2O_5. *J. Phys. Chem. C* **2012**, *116* (22), 12181−12186.
(18) Bayat, F.; Sheibani, S. Enhancement of Photocatalytic Activity of CuO-Cu_2O Heterostructures through the Controlled Content of Cu_2O. *Mater. Res. Bull.* **2022**, *145*, 111561.
(19) Abhilash, M. R.; Akshatha, G.; Srikantaswamy, S. Photocatalytic Dye Degradation and Biological Activities of the Fe_2O_3/Cu_2O Nanocomposite. *RSC Adv.* **2019**, *9* (15), 8557−8568.
(20) Doan, V.-D.; Huynh, B.-A.; Pham, H. A.; Vasseghian, Y.; Le, V. T. Cu_2O/Fe_3O_4/MIL-101(Fe) Nanocomposite as a Highly Efficient and Recyclable Visible-Light-Driven Catalyst for Degradation of Ciprofloxacin. *Environ. Res.* **2021**, *201*, 111593.
(21) Maldonado, M. I.; Saggioro, E.; Peral, J.; Rodríguez-Castellón, E.; Jiménez-Jiménez, J.; Malato, S. Hydrogen Generation by Irradiation of Commercial CuO + TiO_2 Mixtures at Solar Pilot Plant Scale and in Presence of Organic Electron Donors. *Appl. Catal. B Environ.* **2019**, *257*, 117890.
(22) Zhu, J.; Bi, H.; Wang, Y.; Wang, X.; Yang, X.; Lu, L. CuO Nanocrystals with Controllable Shapes Grown from Solution without Any Surfactants. *Mater. Chem. Phys.* **2008**, *109* (1), 34−38.
(23) Kumar, R.; Rai, P.; Sharma, A. Facile Synthesis of Cu_2O Microstructures and Their Morphology Dependent Electrochemical Supercapacitor Properties. *RSC Adv.* **2016**, *6* (5), 3815−3822.
(24) Vivas, L.; Chi-Duran, I.; Enríquez, J.; Barraza, N.; Singh, D. P. Ascorbic Acid Based Controlled Growth of Various Cu and Cu_2O Nanostructures. *Mater. Res. Express* **2019**, *6* (6), 065033.
(25) Wolski, L.; Lebedev, O. I.; Harmer, C. P.; Kovnir, K.; Abdelli, H.; Grzyb, T.; Daturi, M.; El-Roz, M. Unraveling the Origin of Photocatalytic Deactivation in CeO_2/Nb_2O_5 Heterostructure Systems during Methanol Oxidation: Insight into the Role of Cerium Species. *J. Phys. Chem. C* **2021**, *125* (23), 12650−12662.
(26) Jahanara, K.; Farhadi, S. A Magnetically Separable Plate-like Cadmium Titanate-Copper Ferrite Nanocomposite with Enhanced Visible-Light Photocatalytic Degradation Performance for Organic Contaminants. *RSC Adv.* **2019**, *9* (27), 15615−15628.
(27) Issa Hamoud, H.; Wolski, L.; Pankin, I.; Bañares, M. A.; Daturi, M.; El-Roz, M. In Situ and Operando Spectroscopies in Photocatalysis: Powerful Techniques for a Better Understanding of the Performance and the Reaction Mechanism. *Top. Curr. Chem.* **2022**, *380* (5), 37.
(28) Hamoud, H. I.; Douma, F.; Lafjah, M.; Djafri, F.; Lebedev, O.; Valtchev, V.; El-Roz, M. Size-Dependent Photocatalytic Activity of Silver Nanoparticles Embedded in ZX-Bi Zeolite Supports. *ACS Appl. Nano Mater.* **2022**, *5* (3), 3866−3877.
(29) Li, X.; Paier, J. Adsorption of Water on the Fe_3O_4 (111) Surface: Structures, Stabilities, and Vibrational Properties Studied by Density Functional Theory. *J. Phys. Chem. C* **2016**, *120* (2), 1056−1065.
(30) Liu, W.; Zhai, P.; Li, A.; Wei, B.; Si, K.; Wei, Y.; Wang, X.; Zhu, G.; Chen, Q.; Gu, X.; Zhang, R.; Zhou, W.; Gong, Y. Electrochemical CO_2 Reduction to Ethylene by Ultrathin CuO Nanoplate Arrays. *Nat. Commun.* **2022**, *13* (1), 1877.
(31) Chang, X.; Wang, T.; Zhao, Z.; Yang, P.; Greeley, J.; Mu, R.; Zhang, G.; Gong, Z.; Luo, Z.; Chen, J.; Cui, Y.; Ozin, G. A.; Gong, J. Tuning Cu/Cu_2O Interfaces for the Reduction of Carbon Dioxide to Methanol in Aqueous Solutions. *Angew. Chem.* **2018**, *130* (47), 15641−15645.
(32) Deng, B.; Huang, M.; Li, K.; Zhao, X.; Geng, Q.; Chen, S.; Xie, H.; Dong, X.; Wang, H.; Dong, F. The Crystal Plane Is Not the Key Factor for CO_2 to Methane Electrosynthesis on Reconstructed Cu_2O Microparticles. *Angew. Chemie Int. Ed.* **2022**, *61* (7), e202114080.
(33) Perdew, J. P.; Burke, K.; Ernzerhof, M. Generalized Gradient Approximation Made Simple. *Phys. Rev. Lett.* **1996**, *77* (18), 3865−3868.
(34) Kresse, G.; Furthmüller, J. Efficient Iterative Schemes for Ab Initio Total-Energy Calculations Using a Plane-Wave Basis Set. *Phys. Rev. B* **1996**, *54* (16), 11169−11186.
(35) Dudarev, S. L.; Botton, G. A.; Savrasov, S. Y.; Humphreys, C. J.; Sutton, A. P. Electron-Energy-Loss Spectra and the Structural Stability of Nickel Oxide: An LSDA+U Study. *Phys. Rev. B* **1998**, *57* (3), 1505−1509.
(36) Anisimov, V. I.; Elfimov, I. S.; Hamada, N.; Terakura, K. Charge-Ordered Insulating State of Fe_3O_4 from First-Principles Electronic Structure Calculations. *Phys. Rev. B* **1996**, *54* (7), 4387−4390.
(37) Monkhorst, H. J.; Pack, J. D. Special Points for Brillouin-Zone Integrations. *Phys. Rev. B* **1976**, *13* (12), 5188−5192.
(38) Grimme, S. Semiempirical GGA-Type Density Functional Constructed with a Long-Range Dispersion Correction. *J. Comput. Chem.* **2006**, *27* (15), 1787−1799.
(39) Yang, Y.; Xu, D.; Wu, Q.; Diao, P. Cu_2O/CuO Bilayered Composite as a High-Efficiency Photocathode for Photoelectrochemical Hydrogen Evolution Reaction. *Sci. Rep.* **2016**, *6* (1), 35158.
(40) Akizuki, M.; Oshima, Y. Acid Catalytic Properties of TiO_2, Nb_2O_5, and NbO_x/TiO_2 in Supercritical Water. *J. Supercrit. Fluids* **2018**, *141*, 173−181.
(41) Kwon, S.; Lin, T. C.; Iglesia, E. Elementary Steps and Site Requirements in Formic Acid Dehydration Reactions on Anatase and Rutile TiO_2 Surfaces. *J. Catal.* **2020**, *383*, 60−76.
(42) Kwon, S.; Lin, T. C.; Iglesia, E. Formic Acid Dehydration Rates and Elementary Steps on Lewis Acid-Base Site Pairs at Anatase and Rutile TiO_2 Surfaces. *J. Phys. Chem. C* **2020**, *124* (37), 20161−20174.
(43) Zhang, Z.; Liu, K.; Bao, Y.; Dong, B. Photo-Assisted Self-Optimizing of Charge-Carriers Transport Channel in the Recrystallized Multi-Heterojunction Nanofibers for Highly Efficient Photocatalytic H_2 Generation. *Appl. Catal. B Environ.* **2017**, *203*, 599−606.
(44) Issa Hamoud, H.; Damacet, P.; Fan, D.; Assaad, N.; Lebedev, O. I.; Krystianiak, A.; Gouda, A.; Heintz, O.; Daturi, M.; Maurin, G.; Hmadeh, M.; El-Roz, M. Selective Photocatalytic Dehydrogenation of Formic Acid by an In Situ -Restructured Copper-Postmetalated Metal-Organic Framework under Visible Light. *J. Am. Chem. Soc.* **2022**, *144* (36), 16433−16446.
(45) Betancourt-Galindo, R.; Reyes-Rodriguez, P. Y.; Puente-Urbina, B. A.; Avila-Orta, C. A.; Rodríguez-Fernández, O. S.; Cadenas-Pliego, G.; Lira-Saldivar, R. H.; García-Cerda, L. A. Synthesis of Copper Nanoparticles by Thermal Decomposition and Their Antimicrobial Properties. *J. Nanomater.* **2014**, *2014*, 980545.

(46) Inwati, G. K.; Rao, Y.; Singh, M. Thermodynamically Induced in Situ and Tunable Cu Plasmonic Behaviour. *Sci. Rep.* **2018**, *8* (1), 3006.
(47) Ritasalo, R.; Cura, M. E.; Liu, X. W.; Ge, Y.; Kosonen, T.; Kanerva, U.; Söderberg, O.; Hannula, S.-P. Microstructural and Mechanical Characteristics of Cu-Cu_2O Composites Compacted with Pulsed Electric Current Sintering and Hot Isostatic Pressing. *Compos. Part A Appl. Sci. Manuf.* **2013**, *45*, 61−69.
(48) Lany, S. Semiconducting Transition Metal Oxides. *J. Phys.: Condens. Matter* **2015**, *27* (28), 283203.
(49) Parkinson, G. S. Iron Oxide Surfaces. *Surf. Sci. Rep.* **2016**, *71* (1), 272−365.
(50) Marcos-Hernández, M.; Antonio Cerrón-Calle, G.; Ge, Y.; Garcia-Segura, S.; Sánchez-Sánchez, C. M.; Fajardo, A. S.; Villagrán, D. Effect of Surface Functionalization of Fe_3O_4 Nano-Enabled Electrodes on the Electrochemical Reduction of Nitrate. *Sep. Purif. Technol.* **2022**, *282*, 119771.
(51) Aghazadeh, M.; Karimzadeh, I.; Ganjali, M. R.; Malekinezhad, A. Al^{3+} Doped Fe_3O_4 Nanoparticles: A Novel Preparation Method, Structural, Magnetic and Electrochemical Characterizations. *Int. J. Electrochem. Sci.* **2017**, *12* (9), 8033−8044.
(52) Wick, R.; Tilley, S. D. Photovoltaic and Photoelectrochemical Solar Energy Conversion with Cu_2O. *J. Phys. Chem. C* **2015**, *119* (47), 26243−26257.
(53) Kautek, W.; Gordon, J. G. XPS Studies of Anodic Surface Films on Copper Electrodes. *J. Electrochem. Soc.* **1990**, *137* (9), 2672−2677.
(54) Mohamed, M. M.; Bayoumy, W. A.; Goher, M. E.; Abdo, M. H.; Mansour El-Ashkar, T. Y. Optimization of α-Fe_2O_3@Fe_3O_4 Incorporated N-TiO_2 as Super Effective Photocatalysts under Visible Light Irradiation. *Appl. Surf. Sci.* **2017**, *412*, 668−682.
(55) Klab, T.; Luszczynska, B.; Ulanski, J.; Wei, Q.; Chen, G.; Zou, Y. Influence of PEIE Interlayer on Detectivity of Red-Light Sensitive Organic Non-Fullerene Photodetectors with Reverse Structure. *Org. Electron.* **2020**, *77*, 105527.
(56) Pal, S.; Kumar, A.; Kumar, S.; De, A. K.; Prakash, R.; Sinha, I. Visible Light Photocatalysis on Magnetically Recyclable Fe_3O_4/Cu_2O Nanostructures. *Catal. Lett.* **2022**, *152* (11), 3259−3271.
(57) Gerchikov, L. G.; Parshin, D. A.; Shabaev, A. R. Theory of Resonance Saturation of IR Absorption in Semiconductors with Degenerate Resonance Bands in Electric and Magnetic Fields. *Zh. Eksp. Teor. Fiz.* **1989**, *96*, 1046−1065.
(58) Melikyan, A. O.; Minasyan, G. R. Saturation of Interband Absorption in Semiconductors. *Semiconductors* **2000**, *34* (4), 386−388.
(59) Millar, G. J.; Rochester, C. H.; Waugh, K. C. Infrared Study of the Adsorption of Formic Acid on Silica-Supported Copper and Oxidised Copper Catalysts. *J. Chem. Soc. Faraday Trans.* **1991**, *87* (9), 1491−1496.
(60) Nanayakkara, C. E.; Dillon, J. K.; Grassian, V. H. Surface Adsorption and Photochemistry of Gas-Phase Formic Acid on TiO_2 Nanoparticles: The Role of Adsorbed Water in Surface Coordination, Adsorption Kinetics, and Rate of Photoproduct Formation. *J. Phys. Chem. C* **2014**, *118* (44), 25487−25495.
(61) Yu, M.; Trinkle, D. R. Accurate and Efficient Algorithm for Bader Charge Integration. *J. Chem. Phys.* **2011**, *134* (6), 064111.

https://doi.org/10.1021/acscatal.3c04690
ACS Catal. 2023, 13, 16266−16278